Nano Res. 2011, 4(9): 849–860
DOI 10.1007/s12274-011-0141-x
Research Article

ISSN 1998-0124
CN 11-5974/O4

# Nano-Morphology of a Polymer Electrolyte Fuel Cell Catalyst Layer—Imaging, Reconstruction and Analysis

Simon Thiele (✉), Roland Zengerle, and Christoph Ziegler

Laboratory for MEMS Applications, Department of Microsystems Engineering—IMTEK, University of Freiburg, Georges-Koehler-Allee 106, 79110 Freiburg, Germany

Received: 17 February 2011 / Revised: 7 April 2011 / Accepted: 14 April 2011


## ABSTRACT

The oxygen reduction reaction (ORR) in the cathode catalyst layer (CCL) of polymer electrolyte fuel cells (PEFC) is one of the major causes of performance loss during operation. In addition, the CCL is the most expensive component due to the use of a Pt catalyst. Apart from the ORR itself, the species transport to and from the reactive sites determines the performance of the PEFC. The effective transport properties of the species in the CCL depend on its nanostructure. Therefore a three-dimensional reconstruction of the CCL is required. A series of two-dimensional images was obtained from focused ion beam - scanning electron microscope (FIB-SEM) imaging and a segmentation method for the two-dimensional images has been developed. The pore size distribution (PSD) was calculated for the three-dimensional geometry. The influence of the alignment and the anisotropic pixel size on the PSD has been investigated. Pores were found in the range between 5 nm and 205 nm. Evaluation of the Knudsen number showed that gas transport in the CCL is governed by the transition flow regime. The liquid water transport can be described within continuum hydrodynamics by including suitable slip flow boundary conditions.

## KEYWORDS

Cathode catalyst layer (CCL), polymer electrolyte fuel cell (PEFC), tomography, three-dimensional reconstruction

## 1. Introduction

Structural investigations of polymer electrolyte fuel cell (PEFC) components and materials are possible at various scales. For the flow fields, a simple CCD camera can be used to investigate two-phase transport [1]. X-ray analysis and neutron radiography have also been used for this purpose [2, 3]. In the gas diffusion layer, X-ray tomography has been used to image three-dimensional water distributions [4]. Also environmental scanning electron microscopy approaches have been useful for investigating the water dynamics in the gas diffusion layer [5]. For catalyst investigations, transmission electron microscopy (TEM) is regularly used [6]. However, there is no method to investigate the morphology of the cathode catalyst layer (CCL) which is satisfactory for all scales. The oxygen reduction reaction and its related transport processes in the CCL are widely considered to be the major cause of performance losses [7]. Amongst other mechanisms such as charge transfer across the electrochemical double layer and proton transport, these losses are governed by water transport on the micrometre and nanometre scales, the amount of catalyst and its

Address correspondence to Simon.Thiele@imtek.de

distribution. A key role for the quantitative determination of the various transport processes and—in future—for the catalyst distribution is knowledge of the morphology of the pore volume [8].

There are two fundamentally different approaches to obtain a three-dimensional image of the morphology. In stochastic reconstruction, a three-dimensional image is obtained from micro-structural descriptors, which characterise the geometry [9]. From these functions, a geometrical configuration is reconstructed with a mathematical optimisation process. A possible approach is to reconstruct three-dimensional geometries from 2D TEM images [10]. However, the reconstruction quality in this case is limited by the method per se. The Gaussian random fields method can handle only two descriptors. This is not necessarily enough to describe the morphology [11]. A method to overcome this obstacle is simulated annealing [12]. This method has been used for a stochastic reconstruction of a CCL [13]. Here the layer is assumed to consist of overlapping spheres with a certain diameter. Another method in stochastic reconstruction is based on the electrode production process [14]. All phases (ionomer, Pt, carbon and pore) can be addressed. The stochastic reconstruction method is however limited in scope due to the underlying assumptions and does not allow quality control of materials.

The second approach involves experimental input from a real sample and is generally called tomography. A three-dimensional data set of the sample material is obtained experimentally. There is a huge variety of tomographic methods for the sub-micrometre range. For the porous PEFC CCL, the characteristic sizes of the pores range from a few nm to almost one μm [8]. The spatial resolution of X-ray tomographic methods is too low for investigations of the CCL, whereas TEM techniques are better suited for investigations of catalyst features in the range of a few nm since they do not allow visualisation of larger areas. Atomic force microscope tomography does not deliver element information and secondary ion mass spectroscopy tomography does not have enough lateral resolution [15]. focused ion beam - scanning electron microscope (FIB-SEM) tomography has emerged recently [16] and has a spatial resolution between 10 and 1000 nm. It consists of a focused ion beam device (FIB) and a scanning electron microscope (SEM), and has been used for a variety of materials including ceramic fuel cells [17]. However, a three-dimensional reconstruction of a PEFC CCL based on FIB-SEM has not been reported. Our initial results in this area were published in a short communication [18]. Here we describe the whole process from data acquisition to the full three-dimensional geometrical reconstruction in detail. The reconstruction procedure can be subdivided into image acquisition, registration, segmentation and visualisation of the material. We present image acquisition in the Experimental section. Registration, segmentation and visualisation are presented in Results and discussion section. Based on the pore size distribution (PSD), the physics of gas and liquid transport in the CCL is evaluated.

## 2. Experimental

A FuMA-Tech fumapem F-950 membrane, which is a perfluorinated sulphonic acid/PTFE copolymer, was investigated as an example. The electrodes were produced by printing the membrane with a slurry containing 70 wt% platinum on HiSPEC 13100 (Johnson Matthey), a high surface-area carbon support. A 20% Nafion dispersion from DuPont was used as an ionomer and was mixed into the paste in an Ultra Turrax disperser to obtain approximately 20% solid material in the paste. The screen-printing process resulted in a catalyst layer thickness of ca. 2 μm (Fig. 1).

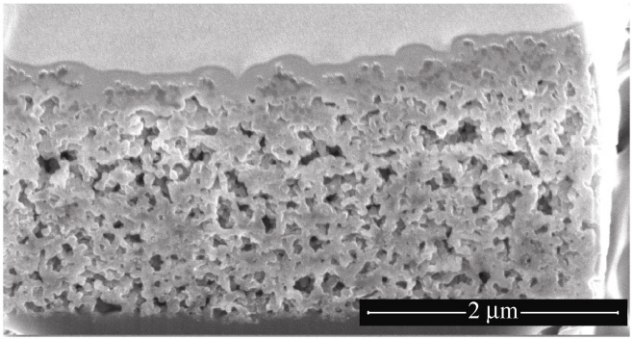


**Figure 1** Typical image from the image series. The porous material is the CCL. The membrane is visible below as the darker grey area. The light grey material above the CCL is the protective Pt layer. It can clearly be seen that the pore morphology close to the protective layer was affected by the deposition. These areas were therefore not considered in the segmentation process. As the images were recorded at an angle of 52°, they are stretched by a factor of 1.27

The catalyst layer was used in the pristine state without any features that are caused by a specific operation protocol.

### 2.1 Image acquisition

The sample was investigated with an FEI Quanta three-dimensional dual-beam FIB-SEM instrument. The first step is preliminary screening of the PEFC CCL layer. Holes and fissures in the micrometre range were found (Fig. 2). Cavities were produced by the ion beam at different micro-homogeneous sample positions. A representative cavity was chosen to perform the reconstruction. In the defect-free areas, the carbon black and ionomer are assumed to be homogeneously mixed. A difference between the carbon and the ionomer phase was unfortunately not observed. This is due to the fact that the molar mass of carbon and the constituent parts of the ionomer are too close to give a good contrast in a SEM device at the present scale. A series of 113 images was made at intervals of 30 nm where the thickness of the layer was about 2 μm. The FIB consisted of $Ga^+$ ions which were accelerated with a voltage of 30 kV. This was followed by SEM imaging of the surface for each slice. One of the images is shown in Fig. 1. The angle of acquisition was 52°. This caused a linear shift of the layer borders between two successive images.

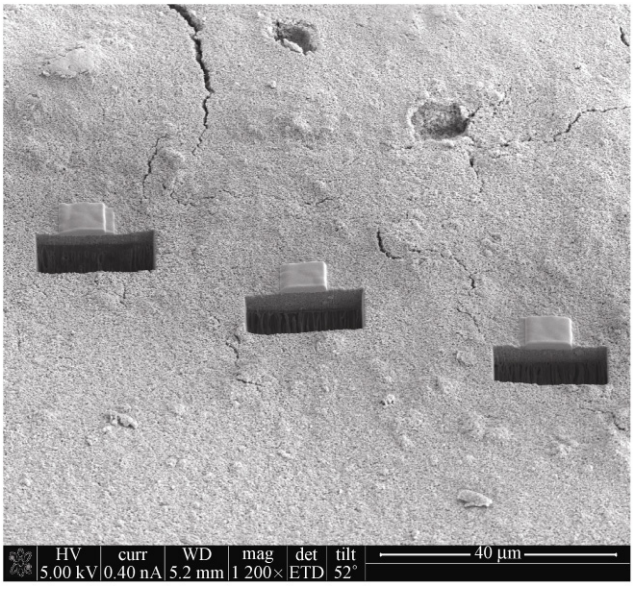


**Figure 2** The cathode surface of the fumapem CCL. Different cavities were created with the ion beam. Two materials are visible in the cavities: The light grey material is the CCL, the darker grey below is the membrane. On top of the CCL, there is a protective Pt layer which also serves as a marker. Micro-homogeneous areas were selected for further investigation

A critical factor determining the precision of the results is the separation of the two-dimensional images in the $z$-direction. The selection of a slicing distance is a trade-off between spatial resolution, acquisition time, segmentation time, cost and slicing precision of the FIB. In the $x$–$y$ direction, the maximal resolution depends on the electron beam. Here, about 1 nm is the state of the art for the resolution [15]. For the $z$-direction, the resolution depends on the ion beam. The resolution limit is in the range of 15 nm [19]. Considering that in the $z$-direction the geometrical scale should be significantly larger than the largest pore diameter of 205 nm and the necessary manual segmentation step, a 30 nm increment was chosen as a compromise between precision, segmentation time and sample size.

### 2.2 Registration

The aligning of successive images is called registration. Due to small variations in the acquisition process, successive images often have an offset. The registration problem for the present data set consists of two parts: In the acquisition process there is a random shift between successive images which is due to small variations of the operating conditions such as fluctuations in the electron optics of the FIB-SEM. The second part is linked to the systematic displacement due to the geometric configuration of the sample and FIB-SEM as the images are taken at an angle of 52° (Fig. 3). There are pore and solid areas in each imaging plane $P_1$, $P_2$. The pore areas contain different information depending on the acquisition angle. Different angles correspond to different pore surface areas (e.g., $A_1$, $A_2$). If we however fix the acquisition angle, a point $R$ in $P_1$ is aligned with a point $R_1$ in $P_2$ instead of being aligned with $R_2$. Therefore the translation algorithm based on a least-squares error estimator only removes stochastic variations between successive images. A shift between images remains. In order to align the images towards Im2 we need a second displacement step.

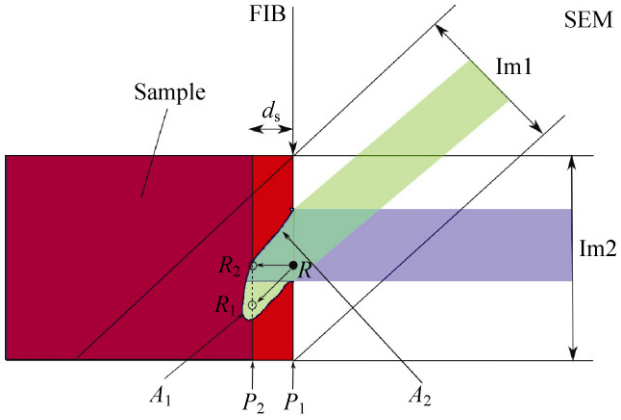


**Figure 3** The geometric configuration of the sample and the FIB-SEM device. The FIB is working at an angle of 52° in relation to the SEM. From the visible image Im1 the image Im2 is reconstructed, which is orthogonal to the FIB plane. The planes $P_1$ and $P_2$ are the planes of successive cuts with a cutting distance of ds. The projection of the visual information from a pore into two different geometrical angles is sketched in blue (Im2) and green (Im1). The information provided by this projection comes from different parts of the pore surface area $A_1$ and $A_2$

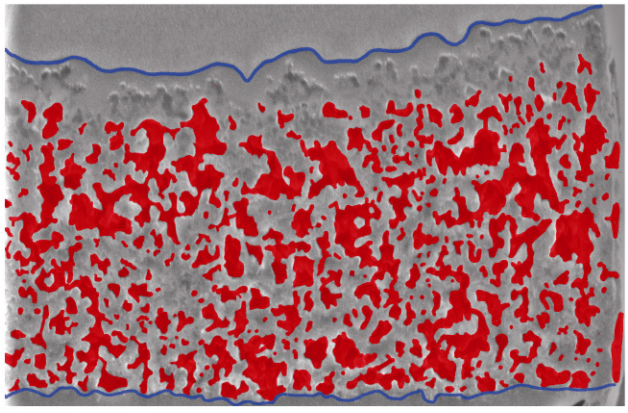

**Figure 4** A stretched and segmented image as an example. The pores have been marked red (colour version)/dark (black and white version). In the upper area, some artefacts from the deposition of the protective layer can be seen. This area was not included in the pore reconstruction as it does not reflect the real pore morphology. In order to correct the image shift, the upper and lower CCL layer lines were marked

This first part of registration was implemented with an ImageJ [20] plug-in (StackReg) which is based on TurboReg [21]. In this module, the registration was performed using the "Translation" option. This means that the image is only shifted as a whole and no local deformation algorithms are used. Afterwards, the images were stretched by a factor of 1.27 corresponding to the acquisition angle of 52°. The second part of the registration consisted in removing the shift between successive images due to the acquisition angle. Here two ways of removing the shift were applied. One way is to mark the upper CCL boundary (Fig. 4), calculate the mean shift between the pixels of successive images and finally shift the images [18]. This way uses a feature in the sample which is clearly visible between successive slides. This method is called "feature registration" in the following. The second way is to shift all images by the slicing distance in *z*-direction multiplied by sin 38°. This simple geometric correction factor stems from the position of the FIB, SEM and sample. This alignment is called "geometric registration". Both alignments will be analysed and compared which may serve as an indication how robust the reconstruction method is in relation to variations in the acquisition process.

### 2.3 Segmentation

Segmentation is the subdivision of the acquired image. Due to its time consumption, it is one of the most important steps in tomography, especially for complex tomographic data [22]. In the present case, the image is divided into porous and solid components (Fig. 4). In the simplest case, the segmentation can be performed by a threshold operation [23]. This is not possible for the material presented here since the grey values for pores and solid material do not differ strongly enough (Fig. 5). One way to surmount this challenge is via manual segmentation. However, the manual segmentation time for the image is unreasonably long; therefore we used a semi-automatic approach, based on pre-selection with an optimised threshold value in the first step and manually improving the results in the second step (Fig. 6). In the first step, an optimised threshold value which is applicable to all 113 images is needed despite three difficulties. There are intensity variations in some parts of the images due to edge effects and the acquisition angle. Secondly, there is a shift in the mean intensity value between successive images due to a general intensity decrease between the first and the last image during the acquisition process. Thirdly, because of the overlapping solid and pore intensity distributions, there are highly

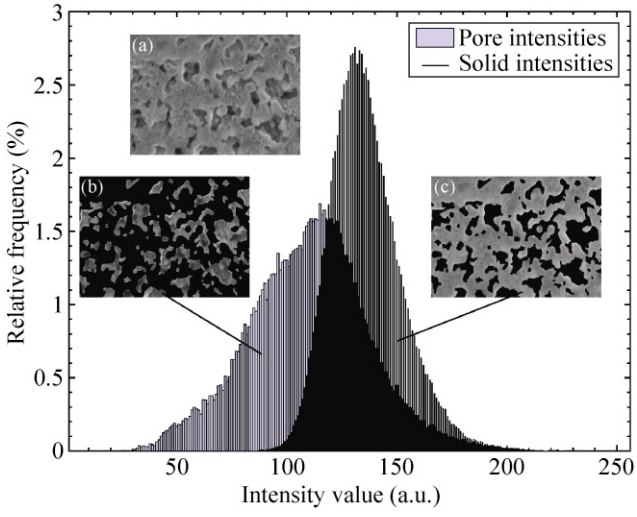


**Figure 5** Intensity distributions of pore (b) and solid (c) components of the original image (a). As the two distributions overlap, automatic threshold segmentation is not possible. With FIB-SEM tomography, not only the information from the cutting plane but also information from inside the pores is part of the image

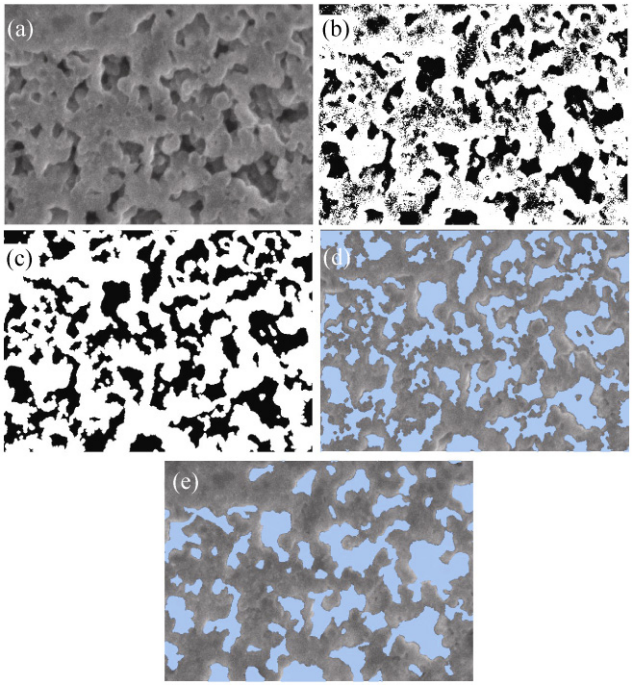


**Figure 6** Segmentation workflow: (a) original image after removing intensity gradients; (b) threshold result for the pore volume. Inhomogeneities remain; (c) after removing the noise and correcting the edges, a very smooth result is obtained; (d) the final mask before manual correction; (e) final manual correction using the software gimp

non-contiguous areas in the image when a threshold value is applied (Fig. 6). The intensity variations are handled by first averaging the original images with a circular filter with a radius of 70 pixels. The averaged image was normalised by dividing each pixel by the image mean value. Finally each pixel from the original image was divided by its corresponding normalised image pixel. The shift in the mean intensity value is removed by shifting all pixel values to a common mean value.

The problem of non-contiguous areas was solved with Matlab's bwareaopen function and a morphological opening (Fig. 6). The difference to simple thresholding is shown in Figs. 6(b) and 6(c). The bwareaopen function removes non-contiguous pixel agglomerates with less than N pixels. After preparing the images in this way, the minimum number N of contiguous pixels and the optimum threshold value were evaluated by comparing the resulting images from the thresholding and opening with manually segmented images. For comparison of manually segmented and automatically processed images, the following similarity measure was chosen: The number of agreements of pore and solid-phase pixels was determined and divided by the overall number of pixels in the image, yielding the percentage of agreement.

The mean agreement in the images was 79%. The final result of this process was an optimum opening area of 80 contiguous pixels and an optimum threshold intensity value of 109. These values were determined on a test set of five manually segmented images. The boundary was smoothed by the morphological opening function, which is a standard image-processing function [24], as a post-processing step which facilitated the manual segmentation. The Matlab imopen function was used with a disk of diameter two as a structuring element. In the second step, the preliminary segmentation results were manually corrected using the open source software gimp (Fig. 6(d)). As a result, 113 segmented images were obtained. A possible way of simplifying the segmentation might be the usage of a pore filling resin given that the pores are filled without a morphology change [25].

### 2.4 Visualisation

For three-dimensional visualisation of porous media, use of Amira® has become the state of the art [19]. The image size from the segmentation is 2048 pixels × 1300 pixels in the $x$–$y$ plane. In order to exclude influences from the boundary layer, e.g., pore morphology change due to the marker deposition and re-deposition (Fig. 4), for the feature registration the images were cut to 1651 pixels × 701 pixels. In the $z$-direction, 113 images were recorded at intervals of 30 nm. The resolution of the images was 2.5 nm/pixel. Hence the three-dimensional geometry is a cuboid with dimensions 4127.5 nm × 1752.5 nm × 3390 nm in the $x$, $y$ and $z$ directions respectively (Fig. 7). The voxel size is 1 pixels × 1 pixels × 12 pixels, corresponding to 2.5 nm × 2.5 nm × 30 nm. The segmented 2D images are provided as tif images in the Electronic Supplementary Material (ESM). The images for the geometric registration were cut to 1760 pixels × 600 pixels thus giving a geometry of 4400 nm × 1500 nm × 3390 nm. Due to the different shifts between the two registration methods the image sizes were different.

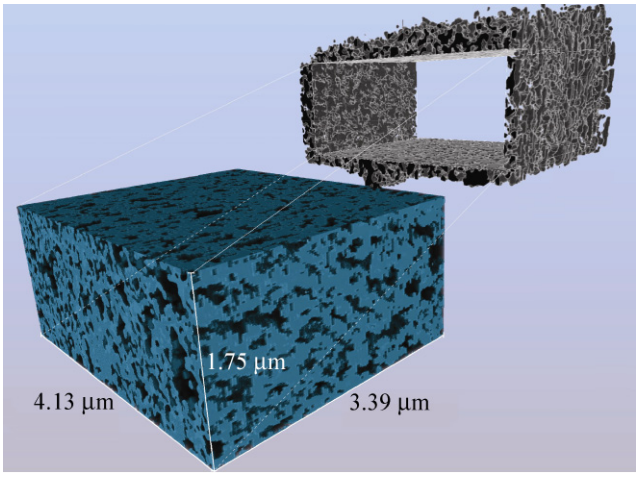


**Figure 7** Three-dimensional geometrical configuration of a polymer electrolyte fuel cell cathode catalyst layer obtained from FIB-SEM imaging. For this geometry the feature registration method was used. The figure shows the carbon matrix morphology (blue in colour version/light grey in black and white version) and the pore network (dark grey) as well as the cut-out process from the segmented region. The result is a statistically well-defined geometry. The largest pore diameter is 205 nm, far less than the side lengths of the geometry

## 3. Results and discussion

### 3.1 Porosity

The connectivity of the pores and the solid material can be evaluated by analysing the connected areas in the geometrical configuration. The bwconncomp function in Matlab with a 26-connected neighbourhood was used for this. This function calculates all connected regions within the sample. The relative amount of ionomer and Pt is not accessible to the FIB-SEM approach. 62% of the volume of the sample consists of solid material, mainly carbon. Correspondingly, pores make up 38% of the sample volume. This is valid for both registration methods. The pore volume fraction of 38% is relatively low compared to highly porous materials with porosities of 65% and above but not unusual for porous electrodes [26]. There are unconnected pores in the sample with a total of 0.21% of the whole volume or 0.56% of the pore volume. To assess the accuracy of these results, the (unphysical) unconnected carbon fraction was determined to be 0.01% of the whole volume only. Again these values are the same for both segmentation methods. It is concluded that artefacts in connectivity, morphology and total volume due to the finite cutting distance (30 nm) and inevitable segmentation errors are in an acceptable range. Moreover the fact that the porosity and connectivity are identical for both registration approaches shows that these values do not strongly depend on the reconstruction procedure.

### 3.2 Pore size distribution

As one of the fundamental properties of porous materials, the PSD of the fumapem CCL was calculated. The approach in Ref. [27] was adopted. The pore sizes are defined as a local concept (Fig. 8 (a)).

For each pixel $P_1$, $P_2$, $P_3$, … which lies within a pore, a sphere is inscribed with a radius equal to the minimum distance to the next pore wall (Fig. 8). In the algorithm, the smaller spheres are inscribed first (e.g., $P_1$). Inscribing larger spheres overwrites part of the previously inscribed spheres (e.g., $P_1$, $P_2$). Finally, each pixel X in the pore is associated with the largest possible sphere surrounding it. The result is a spatial PSD in three dimensions (Fig. 8(b)). A histogram is

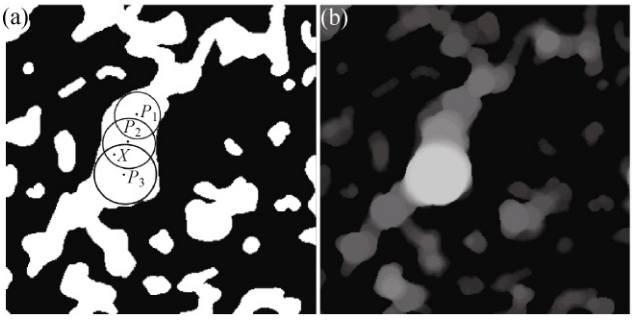


**Figure 8** (a) At every point ($P_1$, $P_2$, …) in the pore structure, a circle is inscribed with a radius equal to the minimum distance to the nearest wall. (b) The resulting spatial pore size distribution

derived from this PSD, yielding the percentage of pixels per pore diameter (Fig. 9). The algorithm was implemented in Matlab. In order to increase the precision of the PSD, a distance transform of the geometry was used instead of a skeleton. This lengthens the calculation time but yields more accurate results. The overall calculation time for the whole geometrical configuration was about three days. The minimum resolution for the PSD is a 5 nm pore diameter, corresponding to the spatial resolution of the 2D SEM images. Additional technical remarks about the implementation can be found in the ESM.

It can be seen that the PSDs for both registrations are in the same range (Fig. 9). 95%/92% (feature registration/geometric registration) of the pore

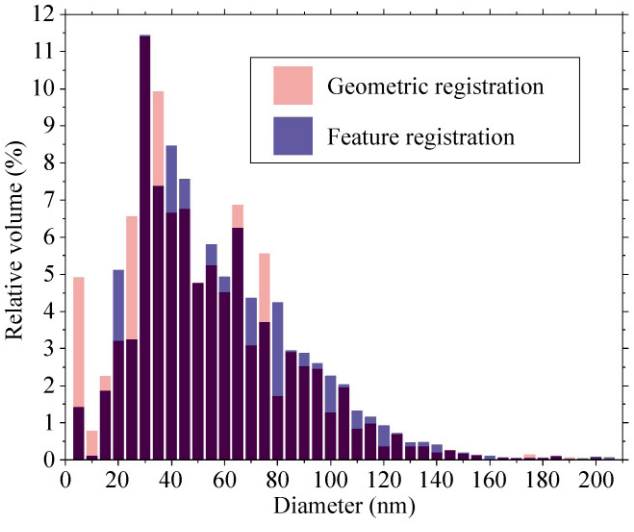


**Figure 9** Pore size distributions for geometric registration and feature registration

diameters are in the range 15 to 120 nm. 77%/76%, however, are between 20 and 80 nm. Thus the catalyst layer is nanoporous rather than microporous. 35%/35% of the pore volume is in the diameter range of 30 to 45 nm. We consider the peak at 5 nm as a numeric artefact, which is more pronounced for geometric registration due to a bigger slope of successive images (see the ESM). We therefore conclude that the PSD calculation is sufficiently robust to errors in the alignment of the images.

In this geometry the resolution is anisotropic: The $x$- and $y$-resolutions were 2.5 nm per pixel and the $z$-resolution was 30 nm per pixel. The anisotropic pixel size implies that there is a different density of morphology information available in the $z$-direction compared with the other directions. Therefore we investigated the dependence of the PSD on the available morphology information in $x$- and $y$-directions keeping the resolution in $z$-direction at 30 nm per pixel. This was done by changing the resolution of the 113 images. In this way the information available in $x$- and $y$-directions was decreased. Comparing the PSD with the maximum resolution of 2.5 nm × 2.5 nm × 30 nm with coarser resolutions can give a qualitative idea of the reliability of the results. The procedure was carried out with the Geometric registration geometry. The images were scaled down by a factor of 12 with the ImageJ scale function. No interpolation or averaging option was used. In this way the minimum morphology information size was set to 30 nm. The resolution for PSD calculation however was kept at the same resolution as in the original geometry in order to make the results comparable (Fig. 10).

At a 30 nm × 30 nm × 30 nm resolution there are still pores found below 30 nm in an amount comparable to a 2.5 nm × 2.5 nm × 30 nm resolution. This result indicates that below 30 nm the values of the 2.5 nm × 2.5 nm × 30 nm resolution PSD are not reliable as they are strongly influenced by pure 2D information. One can further deduce that the results in the 2.5 nm × 2.5 nm × 30 nm resolution PSD for multiples of 30 nm are overly represented due to the cutting distance of 30 nm.

PSDs are often considered to be bimodal [8]. For the present geometry a unimodal distribution was found (Fig. 9). Recently systematic nitrogen adsorption

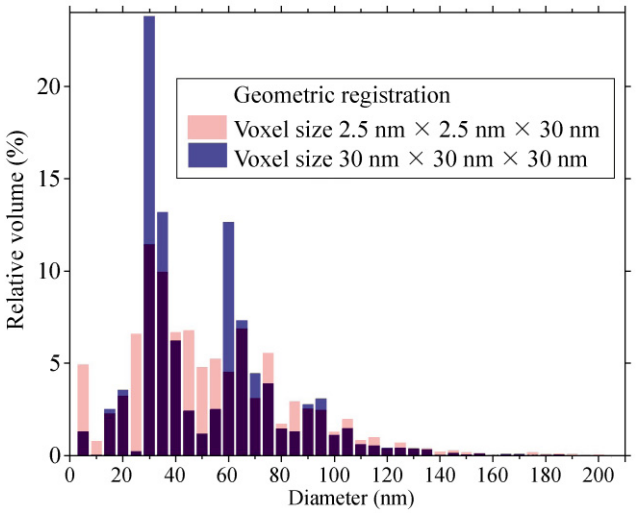


**Figure 10** PSD of the Geometric registration alignment (2.5 nm resolution in the *x*- and *y*-directions, 30 nm in the *z*-direction) and the same geometry with the minimum morphology information size set to 30 nm

measurements of PSDs have been performed [28]. The results show a small maximum below 5 nm and a bigger maximum at 50 to 60 nm. The small maximum however cannot be resolved with the FIB-SEM technique. Therefore no statement about the correctness of this bimodal model can be made. A maximum however can be found in our PSD between 30 to 65 nm. This is in qualitative agreement with the larger maximum from the nitrogen adsorption measurements. For further analysis the feature registration geometry was chosen.

### 3.3 Gas transport in the CCL

The Knudsen number is an established measure for the physical regime of the gas flow as a function of the characteristic pore size. The Knudsen number is defined as

$$Kn \equiv \frac{\lambda}{d} \tag{1}$$

Here $\lambda$ is the mean free path length and d is the pore diameter. For oxygen, $\lambda$ is $6.5\times10^{-8}$ m at ambient conditions [29]. There are four different flow regimes: Continuous flow ($Kn \leqslant 10^{-2}$), slip flow ($10^{-2} < Kn \leqslant 10^{-1}$), transition flow ($10^{-1} < Kn \leqslant 10$) and molecular flow ($Kn > 10$) [30]. The Knudsen numbers in the pores of the fumapem CCL vary between 0.31 (210 nm) and 13 (5 nm). 98.5% of the detected pore volume is subject to the transition flow regime. Pores with a diameter of 5 nm and less are in the molecular regime (Fig. 11).

The Navier–Stokes equations with no-slip boundary conditions are valid for continuous flow [31]. Their validity can be extended to the slip-flow range by taking the slip length into account as a correction term for the boundary conditions [32]. The Knudsen numbers of the CCL presented here, however, indicate that the transition and the molecular regimes are applicable. For this range, particle-based methods such as molecular dynamics (MD), direct simulation Monte Carlo (DSMC) and lattice Boltzmann methods (LBM) are options. The time step in MD simulations however is limited by the size of the interaction potential (e.g., Lennard–Jones Potential).

Thus, in a dilute gas, i.e., for high Knudsen numbers, only a very few interactions occur in one time step. Therefore MD it is not suitable for high Knudsen numbers. The size and morphology of the sample present further challenges for this method. Both DSMC and LBM are based on the Boltzmann equation. In the past, it was doubted that LBM could be used for a Knudsen number range larger than 0.1 [33]. Very recently however, there have been serious efforts to

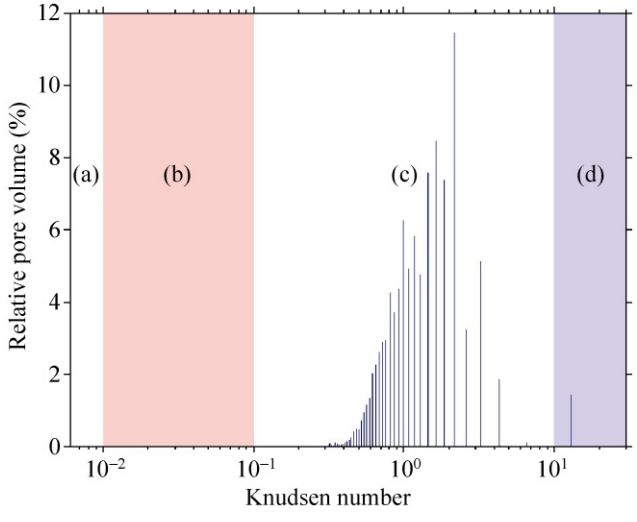


**Figure 11** The gas transport regimes in the pores obtained by plotting the relative pore volume as a function of the Knudsen number: (a) continuous flow; (b) slip flow; (c) transition flow; (d) molecular flow. The figure clearly shows that most of the pore volume is subject to transition flow

extend LBM to Knudsen numbers of 10 and higher in two dimensions [34]. For three dimensions, initial efforts to model transport in the CCL with LBM for this Knudsen number range have been made [13]. Nevertheless, the method which is best established for simulation of rarefied gas dynamics is DSMC [29]. This is underlined by the fact that other methods such as LBM are compared to DSMC for validation in the transition flow regime [33, 34]. DSMC can also be applied to complex porous structures [35]. For an in-depth comparison of DSMC to other methods, see [32].

### 3.4 Liquid transport in the CCL

For the liquid transport, we encounter a more difficult situation without a concept of the same clarity as the well-defined Knudsen number. In the continuum regime, the liquid flow in a circular pore shows the characteristic Poiseuille flow profile [36]. Deviations from the Poiseuille profile are generally taken as an indication of a deviation from Navier-Stokes dynamics [29]. Liquid water transport in confinements has been investigated extensively in the literature. The influence of confinements down to 40 nm for different organic liquids and water has been examined experimentally [37]. The results show that the flow rate obtained does not deviate from the prediction based on the continuum assumption. Other measurements on water showed a viscosity of thin films similar to bulk viscosity down to a thickness of ~1 nm (which is approximately ten molecular diameters) [38, 39]. On the theoretical side, there are several MD simulations which support these results [40, 41]. Therefore it can be stated that the continuum assumption of hydrodynamics for water is valid down to 1–2 nm [29, 42]. This indicates that the liquid water transport in the CCL morphology presented here can be solved within continuum hydrodynamics. It may however be necessary to consider the contact angle hysteresis for the description of free water surfaces and refine the boundary conditions for the flow with a slip length.

The slip length in the pores of different materials is now discussed. The slip length mainly depends on the contact angle $\theta$ which is related to the slip length $b$. The following relation can serve as an estimate [43]:

$$b = \alpha \cdot (1 + \cos\theta)^{-2} \tag{2}$$

with $\alpha = 0.63$ nm [44].

The investigation of slip lengths for different materials is therefore equivalent to investigation of contact angles. The influence of the slip length on the flow through a tube of diameter $d$ depends on both the diameter and the slip length $b$ [45]:

$$S \equiv \frac{Q_{\text{Slip}}}{Q_{\text{Normal}}} = 1 + \frac{8b}{d} \tag{3}$$

where $Q_{\text{Normal}}$ is the flow rate without slip flow and $Q_{\text{Slip}}$ is the slip flow rate. If $S$ becomes larger than one, there is a significant deviation due to slip flow. For investigation of the different materials in the CCL, we assume that mainly the carbon and the ionomer have a strong influence on the slip length as they cover most of the surface. Normally carbon black is used in the CCL. The chemical bonds in carbon black are typically that of graphite ($sp^2$) [46]. For graphite, the contact angle depends very much on the treatment of the material. Accordingly, a complex picture of the water contact angle varying from 0° to over 115° is found in the literature [47]. The greatest share (45%) of measurements can be found between 80°–86°. The extreme values of 0°–29° and 100°–115° both appear with a frequency of 5%. We will therefore compare the values 83°, 14.5°, and 112.5° (Fig. 12). The contact angle of the ionomer depends on its wetting state [48]. The advancing contact angle for a Nafion 117 dry membrane at 97% relative humidity varies between 92° and 103° and for a wet membrane the contact angles varies between 22° and 28° [48]. Therefore we compare the dry case at 97.5° with the wet case at 25° (Fig. 12). For both Nafion and carbon, Eq. (3) is used to make a qualitative comparison although it is clear that this formula can only be a rough estimate.

For carbon, an enhanced flow rate due to slip effects is important in most cases. Interestingly the influence of the slip effects for Nafion strongly depends on its wetting state: In the dry state, 69.8% of the pore volume is significantly ($S > 1.1$) influenced by a slip-enhanced flow rate. In wet states there is almost no influence, with only 3% of the pore volume affected.

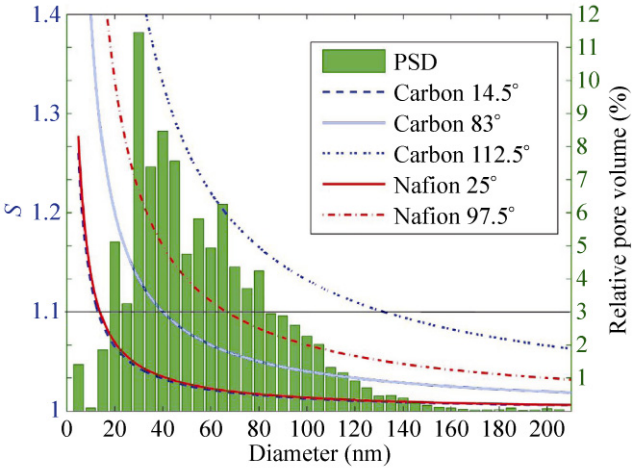


**Figure 12** *S*, the ratio of the slip-enhanced flow to the flow with no slip, as a function of the diameter for different materials and different contact angles. The black horizontal line marks a deviation of 10%. The amount of pore volume showing more than 10% deviation from the normal flow is calculated for the different materials: for carbon at contact angles of 14.5°, 83°, and 112.5°, the amounts of pore volume are 2.7%, 39.2%, and 98.2%, respectively. For dry Nafion (97.5° contact angle), 69.8% of the pore volume is significantly influenced by a slip-enhanced flow rate, whereas for wet Nafion (25° contact angle), this is only the case for 3% of the pore volume

## 4. Conclusions

A three-dimensional reconstruction of a CCL (HiSPEC 13100/Nafion on fumapem F-950) has been demonstrated. A series of 113 2D SEM images was recorded with a separation distance of 30 nm using a FIB. The final voxel size was 2.5 nm × 2.5 nm × 30 nm. By providing open access to the geometry, a new generation of fuel cell modelling founded on the experimentally obtained CCL morphology is made feasible.

A semi-automatic segmentation procedure has been developed, which consists of a normalisation procedure for a global threshold value applicable to all images and a manual segmentation step afterwards.

The PSD was determined according to Delerue [27]. Pores were found with diameters between 5 and 205 nm, the lower limit being determined by the resolution limit of the SEM images. A variation of the image resolution revealed that PSD values below 30 nm are not reliable. 95% of the pore volume is distributed among pores with 15 to 120 nm diameter. 80% of the volume, however, has diameters between 20 to 80 nm, which shows the overall nanoporous characteristics of the layer. The maximum of the PSD is between 30 to 45 nm, with 35% of the pore volume in this range. A comparison of two different alignment methods showed that the porosity, connectivity and PSD calculation are sufficiently robust to alignment variations.

An analysis of the Knudsen number regime showed that the gas transport in the pores is governed by the transition flow regime. For liquid transport, it is concluded that continuum hydrodynamics is a valid approach.

Slip flow is generally important if liquid water is in contact with the carbon matrix of the CCL. Where the pore walls are covered with Nafion in its dry state slip flow is also non-negligible, whereas for pores covered with Nafion in the wet state, slip flow can be safely neglected.

Based on these results, suggestions for future research work include improvement of the segmentation process, development of transition flow gas transport models for the CCL and description of liquid transport including slip flow and contact angle dynamics.

## Acknowledgements

This work was supported by the German Research Foundation (DFG) under grant No. ZI 1201/2-2. The authors acknowledge the fruitful collaboration with H. Blumtritt (Max Planck Institute for Microstructure Physics) and M. Buchheim (HIAT GmbH).

**Electronic Supplementary Material**: The complete feature registration reconstruction geometry as a series of tif images is available in the online version of this article. One image is given for each slice. In order to obtain the original geometry, every slice has to be repeated twelve times. Additional technical remarks on the implementation can also be found. This material is available at: http://dx.doi.org/10.1007/s12274-011-0141-x.

## References

[1] Yang, H.; Zhao, T. S.; Ye, Q. Pressure drop behavior in the anode flow field of liquid feed direct methanol fuel cells. *J.*

*Power Sources* **2005**, *142*, 117–124.

[2] Manke, I.; Hartnig, C.; Gruenerbel, M.; Lehnert, W.; Kardjilov, N.; Haibel, A.; Hilger, A.; Banhart, J.; Riesemeier, H. Investigation of water evolution and transport in fuel cells with high resolution synchrotron X-ray radiography. *Appl. Phys. Lett.* **2007**, *90*, 174105.

[3] Schroeder, A.; Wippermann, K.; Mergel, J.; Lehnert, W.; Stolten, D.; Sanders, T.; Baumhöfer, T.; Sauer, D. U.; Manke, I.; Kardjilov, N. Combined local current distribution measurements and high resolution neutron radiography of operating direct methanol fuel cells. *Electrochem. Commun.* **2009**, *11*, 1606–1609.

[4] Sinha, P. K.; Halleck, P.; Wang, C. Y. Quantification of liquid water saturation in a PEM fuel cell diffusion medium using X-ray microtomography. *Electrochem. Solid-state Lett.* **2006**, *9*, A344–A348.

[5] Ziegler, C.; Gerteisen, D. Validity of two-phase polymer electrolyte membrane fuel cell models with respect to the gas diffusion layer. *J. Power Sources* **2009**, *188*, 184–191.

[6] Xie, Z.; Navessin, T.; Shi, K.; Chow, R.; Wang, Q.; Song, D.; Andreaus, B.; Eikerling, M.; Liu, Z.; Holdcroft, S. Functionally graded cathode catalyst layers for polymer electrolyte fuel cells. *J. Electrochem. Soc.* **2005**, *152*, A1171–A1179.

[7] Gerteisen, D.; Heilmann, T.; Ziegler, C. Modeling the phenomena of dehydration and flooding of a polymer electrolyte membrane fuel cell. *J. Power Sources* **2009**, *187*, 165–181.

[8] Eikerling, M. Water management in cathode catalyst layers of PEM fuel cells. *J. Electrochem. Soc.* **2006**, *153*, E58–E70.

[9] Torquato, S.; Haslach, H. W. Jr. *Random Heterogeneous Materials: Microstructure and Macroscopic Properties;* Springer: New York, 2002.

[10] Mukherjee, P. P.; Wang, C. Y. Direct numerical simulation modeling of bilayer cathode catalyst layers in polymer electrolyte fuel cells. *J. Electrochem. Soc.* **2007**, *154*, B1121–B1131.

[11] Levitz, P. Off-lattice reconstruction of porous media: Critical evaluation, geometrical confinement and molecular transport. *Adv. Colloid .Interf. Sci.* **1998**, *76*, 71–106.

[12] Torquato, S. Statistical description of microstructures. *Annu. Rev. Mater. Res.* **2002**, *32*, 77–111.

[13] Kim, S. H.; Pitsch, H. Reconstruction and effective transport properties of the catalyst layer in PEM fuel cells. *J. Electrochem. Soc.* **2009**, *156*, B673–B681.

[14] Siddique, N. A.; Liu, F. Process based reconstruction and simulation of a three-dimensional fuel cell catalyst layer. *Electrochim. Acta* **2010**, *55*, 5357–5366.

[15] Möbus, G.; Inkson, B. J. Nanoscale tomography in materials science. *Mater. Today* **2007**, *10*,18–25.

[16] Holzer, L.; Indutnyi, F.; Gasser, P. H.; Munch, B.; Wegmann, M. Three-dimensional analysis of porous $BaTiO_3$ ceramics using FIB nanotomography. *J. Microscopy* **2004**, *216*, 84–95.

[17] Wilson, J. R.; Kobsiriphat, W.; Mendoza, R.; Chen, H. Y.; Hiller, J. M.; Miller, D. J.; Thornton, K.; Voorhees, P. W.; Adler, S. B.; Barnett, S. A. Three-dimensional reconstruction of a solid-oxide fuel-cell anode. *Nat. Mater.* **2006**, *5*, 541–544.

[18] Ziegler, C.; Thiele, S.; Zengerle, R. Direct three-dimensional reconstruction of a nanoporous catalyst layer for a polymer electrolyte fuel cell. *J. Power Sources* **2011**, *196*, 2094–2097.

[19] Holzer, L.; Muench, B.; Wegmann, M.; Gasser, P.; Flatt, R. J. FIB-nanotomography of particulate systems—Part I: Particle shape and topology of interfaces. *J. Amer. Ceram. Soc.* **2006**, *89*, 2577–2585.

[20] Abramoff, M. D.; Magalhaes, P. J.; Ram, S. J. Image processing with ImageJ. *Biophoton. Int.* **2004**, *11*, 36–43.

[21] Thevenaz, P.; Ruttimann, U. E.; Unser, M. A pyramid approach to subpixel registration based on intensity. *IEEE Trans. Image Process.* **1998**, *7*, 27–41.

[22] Pal, N. R.; Pal, S. K. A review on image segmentation techniques. *Pattern Recog.* **1993**, *26*,1277–1294.

[23] Munch, B.; Gasser, P.; Holzer, L.; Flatt, R. FIB-Nanotomography of particulate systems—Part II: Particle recognition and effect of boundary truncation. *J. Amer. Ceram. Soc.* **2006**, *89*, 2586–2595.

[24] Ohser, J.; Mücklich, F. *Statistical Analysis of Microstructures in Materials Science;* John Wiley: New York, 2000.

[25] Wilson, J. R.; Cronin, J. S.; Barnett, S. A.; Harris, S. J. Measurement of three-dimensional microstructure in a $LiCoO_2$ positive electrode *J. Power Sources* **2011**, *196*, 3443–3447.

[26] Fischer, A.; Jindra, J.; Wendt, H. Porosity and catalyst utilization of thin layer cathodes in air operated PEM-fuel cells. *J. Appl. Electrochem.* **1998**, *28*, 277–282.

[27] Delerue, J. F.; Perrier, E.; Yu, Z. Y.; Velde, B. New algorithms in 3D image analysis and their application to the measurement of a spatialized pore size distribution in soils. *Phys. Chem Earth A: Solid Earth Geodesy* **1999**, *24*, 639–644.

[28] Soboleva, T.; Zhao, X.; Malek, K.; Xie, Z.; Navessin, T.; Holdcroft, S. On the micro-, meso-, and macroporous structures of polymer electrolyte membrane fuel cell catalyst layers. *ACS Appl. Mater. Interf.* **2010**, *2*, 375–384.

[29] Karniadakis, G.; Beskok, A.; Aluru, N. R. *Microflows and Nanoflows: Fundamentals and Simulation;* Springer Verlag: Berlin, 2005.

[30] Schaaf , S. A.; Chambré, P. L. *Flow of Rarefied Gases;* Princeton University Press: Princeton, 1961.

[31] Gad-El-Hak, M. Gas and liquid transport at the microscale. *Heat Transf. Eng.* **2006**, *27*, 13–29.

[32] Oran, E. S.; Oh, C. K.; Cybyk, B. Z. Direct simulation Monte Carlo: Recent advances and applications. *Annu. Rev. Fluid Mech.* **1998**, *30*, 403–441.

[33] Shen, C.; Tian, D. B.; Xie, C.; Fan, J. Examination of the LBM in simulation of microchannel flow in transitional regime. *Nanoscale Microscale Thermophys. Eng.* **2004**, *8*, 423–432.

[34] Kim, S. H.; Pitsch, H.; Boyd, I. D. Lattice Boltzmann modeling of multicomponent diffusion in narrow channels. *Phys. Rev. E* **2009**, *79*, 16702.

[35] Zalc, J. M.; Reyes, S. C.; Iglesia, E. Monte Carlo simulations of surface and gas phase diffusion in complex porous structures. *Chem. Eng. Sci.* **2003**, *58*, 4605–4617.

[36] Johnson, R. W. *The Handbook of Fluid Dynamics;* Springer: Heidelberg, 1998.

[37] Cheng, J. T.; Giordano, N. Fluid flow through nanometer-scale channels. *Phys. Rev. E* **2002**, *65*, 31206.

[38] Raviv, U.; Laurat, P.; Klein, J. Fluidity of water confined to subnanometre films. *Nature* **2001**, *413*, 51–54.

[39] Raviv, U.; Klein, J. Fluidity of bound hydration layers. *Science* **2002**, *297*, 1540–1543.

[40] Leng, Y.; Cummings, P. T. Fluidity of hydration layers nanoconfined between mica surfaces. *Phys. Rev. Lett.* **2005**, *94*, 26101.

[41] Thomas, J. A.; McGaughey, A. J. H. Water flow in carbon nanotubes: Transition to subcontinuum transport. *Phys. Review Lett.* **2009**, *102*, 184502.

[42] Bocquet, L.; Charlaix, E. Nanofluidics, from bulk to interfaces. *Chem. Soc. Rev.* **2010**, *39*, 1073–1095.

[43] Huang, D. M.; Sendner, C.; Horinek, D.; Netz, R. R.; Bocquet, L. Water slippage versus contact angle: A quasiuniversal relationship. *Phys. Rev. Lett.* **2008**, *101*, 226101.

[44] Sendner, C.; Horinek, D.; Bocquet, L.; Netz, R. R. Interfacial water at hydrophobic and hydrophilic surfaces: Slip, viscosity, and diffusion. *Langmuir* **2009**, *25*, 10768–10781.

[45] Tandon, V.; Kirby, B. J. Zeta potential and electroosmotic mobility in microfluidic devices fabricated from hydrophobic polymers: 2. Slip and interfacial water structure. *Electrophoresis* **2008**, *29*, 1102–1114.

[46] Jawhari, T.; Roid, A.; Casado, J. Raman spectroscopic characterization of some commercially available carbon black materials. *Carbon* **1995**, *33*, 1561–1565.

[47] Mattia, D.; Gogotsi, Y. Review: Static and dynamic behavior of liquids inside carbon nanotubes. *Microfluid. Nanofluid.* **2008**, *5*, 289–305.

[48] Bass, M.; Berman, A.; Singh, A.; Konovalov, O.; Freger, V. Surface structure of Nafion in vapor and liquid. *J. Phys. Chem. B* **2010**, *114*, 3784–3790.